

Supplementary Information

Surface Charge Enhanced Carbon Electrodes for Stable and Efficient Capacitive Deionization Using Inverted Adsorption-Desorption Behavior

Xin Gao,^a Ayokunle Omosebi,^a James Landon,^{a*} and Kunlei Liu,^{ab*}

^aCenter for Applied Energy Research, University of Kentucky, Lexington, KY 40511, USA.

^bDepartment of Mechanical Engineering, University of Kentucky, Lexington, KY 40506, USA.

Email: James.Landon@uky.edu; Fax: +1 859 257 0302; Tel: +1 859 257 0349

Email: Kunlei.Liu@uky.edu; Fax: +1 859 257 0302; Tel: +1 859 257 0293

1. Introduction

In this section, we provide the supporting documents indicated in the main text. Specifically, we will discuss the ‘V-shape’ formed in the voltammograms associated with the carbon xerogel (CX), Zorflex (ZX), and Spectracarb (SC) electrodes based upon the Gouy-Chapman-Stern (GCS) model for the electrochemical double layer (EDL), and the impact of oxygen-containing functional groups at the carbon surface on the relocation of the potential of zero charge (E_{PZC}). In addition, through a long-term CDI test, a

mechanism for salt separation performance will be shown based upon shifting of the E_{PZC} with respect to the potential distribution.

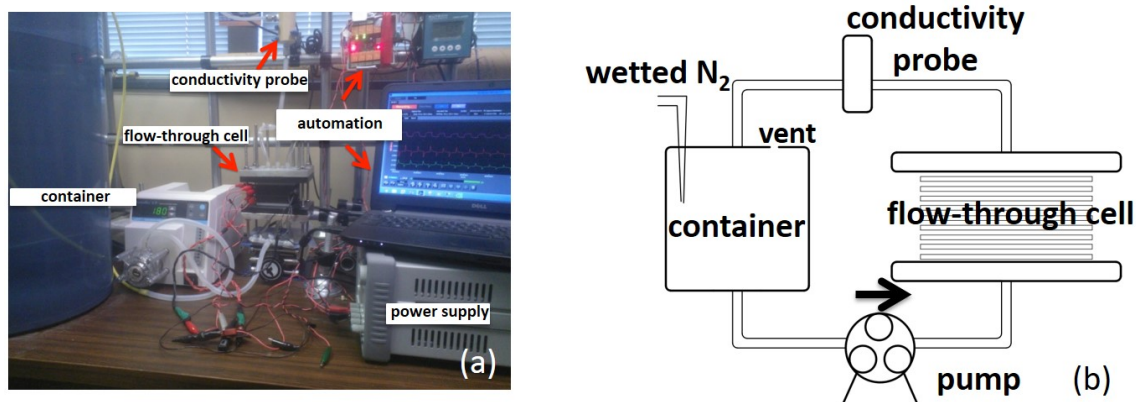


Figure S1. The flow system pictured was used to examine CX and other carbon electrodes for CDI applications.

2. Experimental

2.1 Flow System and Flow-Through Cell

Fig. S1(a)-(b) shows a picture of the flow cell system used in the study and a schematic of the same system, respectively. Separation performance of the CX, ZX, and SC materials was investigated in a flow-through CDI cell. Each electrode had an effective geometric area of $\sim 23 \text{ cm}^2$ (corresponding to $\sim 0.5 \text{ g}$) and was contacted by means of a titanium current collector. The space between the cathode and anode was 1.5 mm using silicone rubber spacers only. During system operation, 31 L (or 2 L) of 4.3 mM NaCl solution was continuously purged with wetted N₂ in the solution container and circulated at a flow rate of $\sim 75 \text{ mL min}^{-1}$ using a peristaltic pump (Masterflex) at room temperature.

A conductivity meter (Cole-Parmer 19500-45) at the flow cell outlet was installed for calculation of the electrosorption capacity (the Γ value). It should be noted that before wetting the cell, short-circuiting between electrodes was examined using a multimeter (RadioShack).

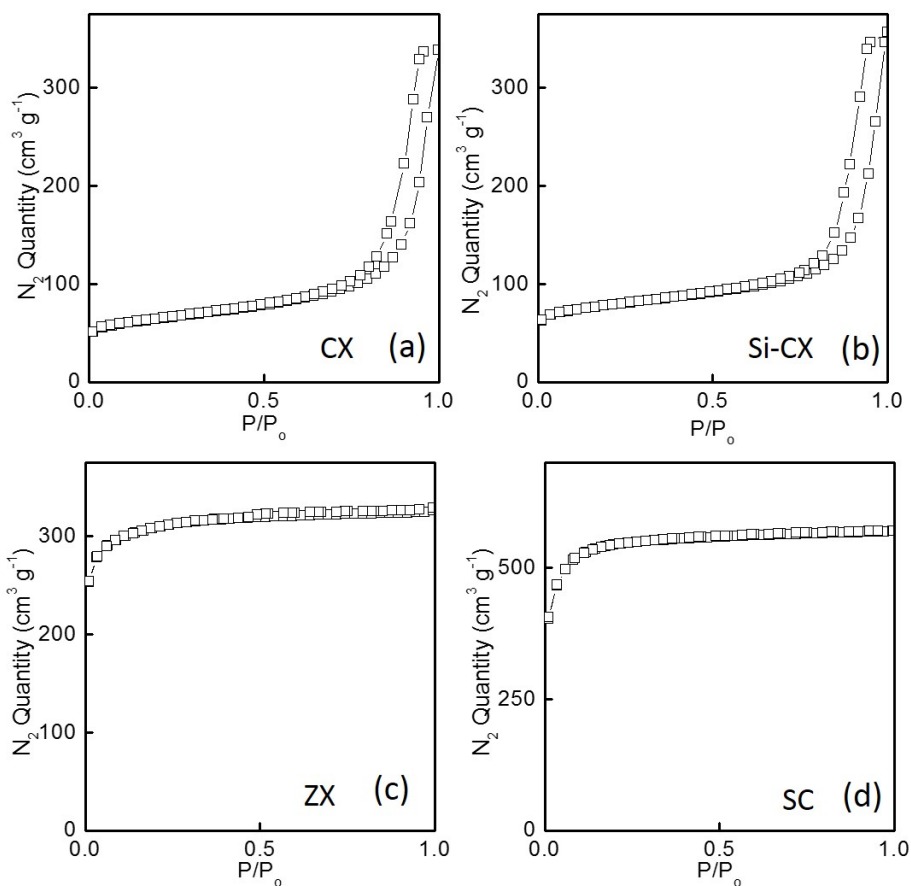


Figure S2. The N_2 adsorption-desorption isotherms for the (a) CX, (b) Si-CX, (c) ZX, and (d) SC materials. The ZX and SC materials are commercially available at www.chemvironcarbon.com and www.caplinq.com, respectively.

3. Results

3.1. N₂ Adsorption-Desorption Isotherms for CX, Si-CX, ZX, and SC Materials

The porosity measurements were carried out under N₂ atmosphere using a porosity and surface area analyzer (ASAP 2020, Micrometrics). As shown in Fig. S2(a)-(b), since no rapid increase is seen for N₂ adsorption at low pressure (e.g., $P/P_0 < 0.3$), and a hysteresis loop is formed at high pressure, it can be understood that the CX and Si-CX materials are mainly mesoporous.¹ Therefore, the Barrett-Joyner-Halenda (BJH) method was selected to quantify the incremental pore volume and the cumulative pore volume displayed in the main text based upon these isotherms. As shown in the pore size distributions in Fig. 3(a)-(b) in the main text, we consider that the modification does not lead to significant changes in the pore structure and pore volume.

Monolithic carbon cloths, ZX and SC, were also purchased to compare to the CX materials prepared in our lab. Unlike mesoporous CX materials, these carbon cloths are composed of a large number of micropores as a sharp increase in N₂ adsorption at a low relative pressure is observed in its isotherms in Fig. S2(c)-(d),¹ which results in a total pore volume of ~ 0.50 and ~ 0.88 cm³ g⁻¹ and a specific surface area of about ~ 900 and ~ 1700 m² g⁻¹ for the ZX and SC materials, respectively.

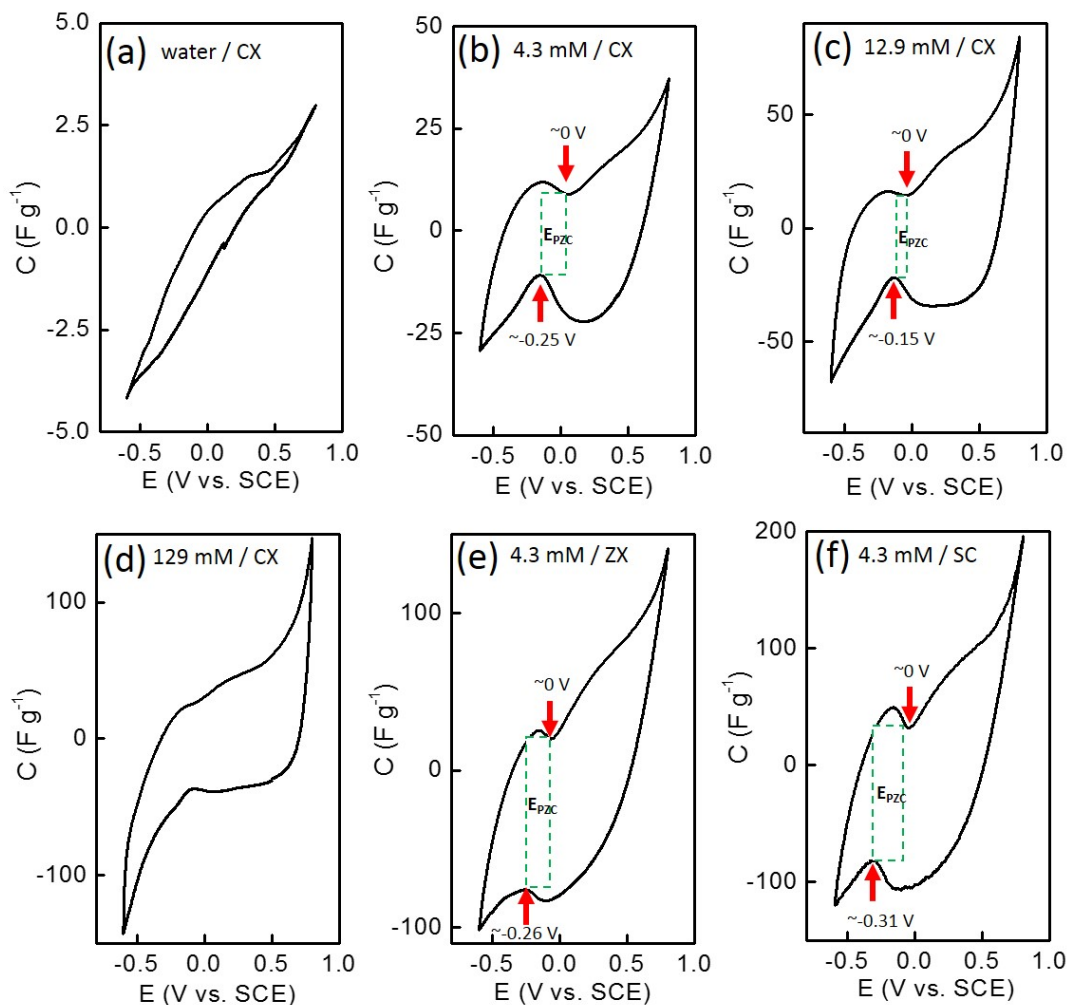


Figure S3. Cyclic voltammetry performed at 1 mV s^{-1} for pristine CX electrodes in deaerated NaCl solution of different concentrations including the use of (a) deionized water, (b) 4.3 mM, (c) 12.9 mM, and (d) 129 mM to verify the ‘V-shape’ formed in voltammograms predicted by the Gouy-Chapman-Stern (GCS) model for the electrochemical double-layer. Cyclic voltammetry was also performed at 0.25 mV s^{-1} in 4.3 mM deaerated NaCl solution when the commercially available (e) ZX and (f) SC electrodes were examined. In these plots, capacitance (C) was calculated using $C = j / v$, where j is the current density and v is the voltage scan rate.

3.2. 'V-Shape' in Voltammograms

3.2.1. Effect of Salt Concentration

According to the Gouy-Chapman-Stern (GCS) model for the electrochemical double-layer, the reciprocal of the capacitance at an electrode (C_d) is the summation of the reciprocals of the component capacitances (Eq. [1]), i.e., the capacitance of the charge held at the outer Helmholtz plane (C_H) and the capacitance of the diffuse layer (C_D).

$$1/C_d = 1/C_H + 1/C_D \quad [1]$$

Unlike the linear behavior of the C_H value, the C_D value shows a 'V-shape' when potential vs. capacitance is plotted.² Since the C_d value is always governed by the smaller of the C_H and C_D values, the 'V-shape' will be observed if a small solution concentration is used in accordance with the GCS prediction, which could be verified by cyclic voltammetry or electrochemical impedance spectroscopy.³⁻⁸

The resulting voltammograms for the CX electrode in NaCl solution are consistent with the GCS predication. As shown in the voltammograms of Fig. S3, the 'V-shape' in a plot of capacitance versus potential (highlighted by rectangles) becomes very distinct for a pristine electrode when 4.3 and 12.9 mM NaCl solutions were used (Fig. S3(b) and (c)). However, this similarity becomes less apparent when the solution was replaced by 129 mM NaCl solution and deionized water (Fig. S3(d) and (a)). Bard and Faulkner summarized that at the 'V-shape' in the plot of capacitance versus potential, a potential at which zero surface charge exists, which is named the potential of zero charge (E_{PZC}).² This characteristic potential at the electrode can be recognized as a transition stage for the surface charge, e.g., cation-adsorption occurs as the applied potential

negatively passes the E_{PZC} , and vice versa.⁸ We consider that, unlike a redox flow battery or a fuel cell, the potential distribution in a CDI cell is difficult to predict thermodynamically due to the lack of substantial electrochemically active redox species. However, due to the impact of the E_{PZC} on adsorption-desorption, knowledge of its location with respect to the electrode's working domain is critical to the electrosorption performance of a CDI cell.^{9, 10}

Like CX materials, Fig. S3(e)-(f) shows that the ZX and SC electrodes also have a distinct 'V-shape' marked by rectangles in their voltammograms. Thus, the electrosorption performance for CDI cells with ZX and SC electrodes will be similar to that for the CX electrode, and their cycling performance will be shown later in the supplementary information.

It is also found that the 'V-shape' regions associated with the anodic and cathodic branches are deviated for all the tested electrodes in the dilute salt solutions. This deviation is due to the relatively high resistance at the interface between the electrodes and the solution, and the dependence of the E_{PZC} measurement on transient conditions, leading to the need for lower voltage scan rates to obtain better resolution.¹¹ In this study, the E_{PZC} is estimated by averaging the location of the 'V-shape' at the cathodic and anodic branches in the voltammograms. For instance, the E_{PZC} for the pristine CX in 4.3 mM NaCl is ~ -0.13 V vs. SCE.

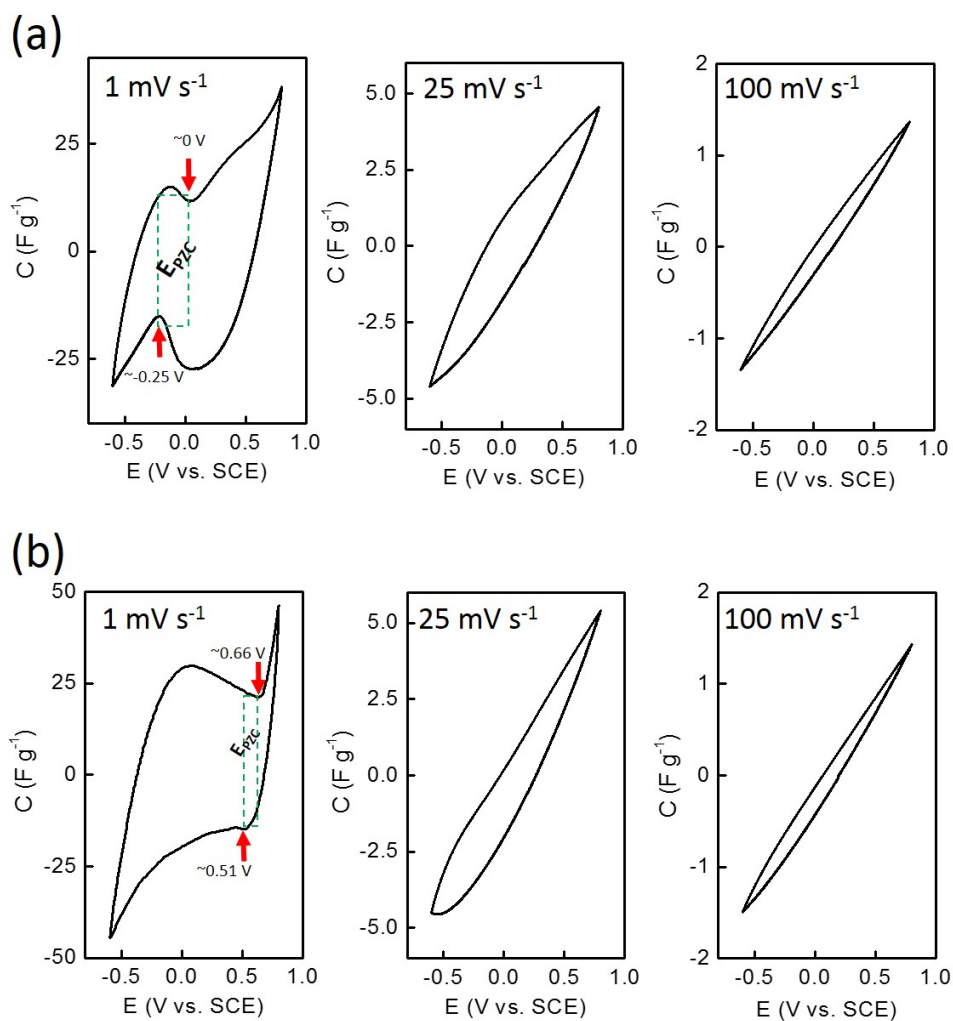


Figure S4. Cyclic voltammetry performed at different scan rates using (a) pristine CX and (b) Si-CX electrodes in 4.3 mM deaerated NaCl solution. In these plots, capacitance (C) was calculated using $C = j / v$, where j is the current density and v is the voltage scan rate.

3.2.2. Effect of Scan Rate

Fig. S4 shows the cyclic voltammograms for the pristine CX and Si-CX electrodes at 1, 25, and 100 mV s⁻¹ in 4.3 mM deaerated NaCl solution. It is found that an increase in the scan rate results in the 'V-shape' in the voltammograms vanishing and the overall

capacitance (i.e., area under the curve) being smaller. This observation suggests that the examination of the E_{PZC} location has to be performed at a low scan rate. Furthermore, we consider that the ‘V-shape’ formed at low scan rate may be dependent on the pore size distribution for the tested carbon electrodes.^{11 12} In addition, the effect of voltage scan rates indicates that the E_{PZC} measurement by cyclic voltammetry is not an artifact due to electrochemical reactions.

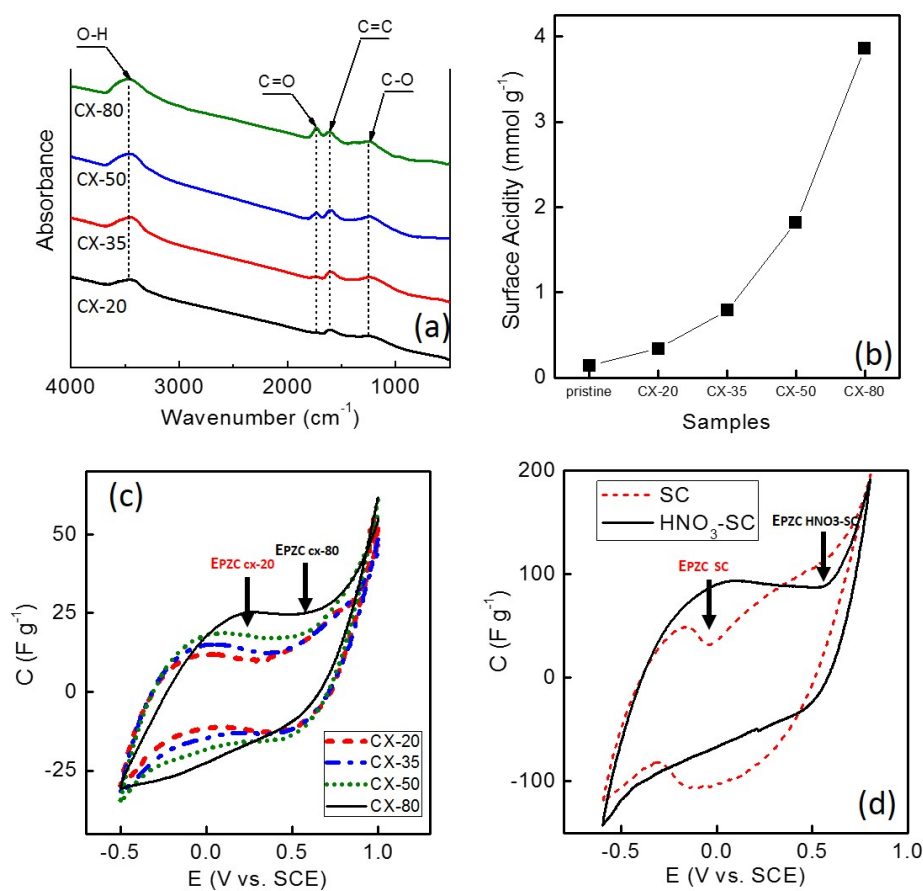


Figure S5. Characterization of carbon materials treated in concentrated HNO₃. (a) The FTIR spectra for the CX-20 – 80 materials. (b) The surface acidity of the CX-20 – 80 materials. (c) The voltammograms for the CX-20 – 80 electrodes at 0.5 mV s⁻¹ in 4.3 mM

deaerated NaCl solution. (d) The voltammograms for the SC and HNO₃-SC electrodes at 0.25 mV s⁻¹ in 4.3 mM deaerated NaCl solution.

3.3. E_{PZC} Relocation

3.3.1. Positive E_{PZC} Shifting by Oxidation

The procedure for the HNO₃-treatment is as follows. A graduated cylinder with a film cover was used to heat 300 cm³ of ~70% HNO₃ (Acros) in a temperature-controlled coolant bath (Thermo Scientific). When the temperature of HNO₃ was stable (at 20, 35, 50 and 80°C), a CX sheet with a geometric area of ~50 cm² was placed into the cylinder for 1 hour. After treatment, to remove any residual HNO₃ on the surface of the carbon, the treated carbon was washed with a copious amount of deionized water until the pH value of the wash solution approached neutral. Subsequently, the wet carbon was post-treated at 160°C overnight in a vacuum oven before testing. To facilitate analysis, the treated CX materials are labeled as CX-20, -35, -50 and -80, representing CX that was treated in HNO₃ at different temperatures, e.g., CX-20 means that a CX sheet was treated at 20°C.

Fig. S5(a) shows the effect of treatment temperature on the FTIR spectra. It can be seen that an increase in the treatment temperature results in an increase in the relative ratio of the absorbance at ~1730 and ~1600 cm⁻¹. This indicates that the formation of oxygen-containing groups (e.g., carboxylic groups) can be enhanced by an increase in the treatment temperature.¹³ This result also suggests that the CX material has been oxidized to different degrees by treatment at different temperatures. To quantify the oxygen-containing functional groups (oxidation degree), we performed a 0.015 M NaOH titration

to determine the amount of total acidity on the CXs under investigation.^{14, 15} The results are plotted in Fig S5(b). It can be seen that an increase in the treatment temperature leads to an increase in the total acidity. Cyclic voltammetry was performed on these electrodes at 0.5 mV s⁻¹ in 4.3 mM deaerated NaCl solution, and the voltammograms are shown in Fig. S5(c). In general, it is found that the ‘V-shape’ highlighted by arrows is positively shifted with increases in the surface acidity or oxygen-containing functional groups. In Fig. S5(d), similar movement of the ‘V-shape’ in the voltammogram can be observed when the commercially available SC electrode was treated in concentrated HNO₃. Thus, it can be concluded that an increase in the oxygen-containing functional groups will result in the E_{PZC} being positively shifted for most carbon electrodes, which has been studied by Tobias and Soffer.¹⁶

3.3.2. Relationship between E_{PZC}, pH_{PZC}, and ζ-Potential

We quote the definition of the point of zero charge (pH_{PZC}) and the potential of zero charge (E_{PZC}) by McCafferty, which reported that “the E_{PZC} determines how the charge on an oxide film responds to changes in electrode potential of the oxide-covered electrode whereas the pH_{PZC} reflects how the charge on an oxide film responds to changes in pH of the solution.”¹⁷ These two parameters can be linked to the zeta potential (ζ),

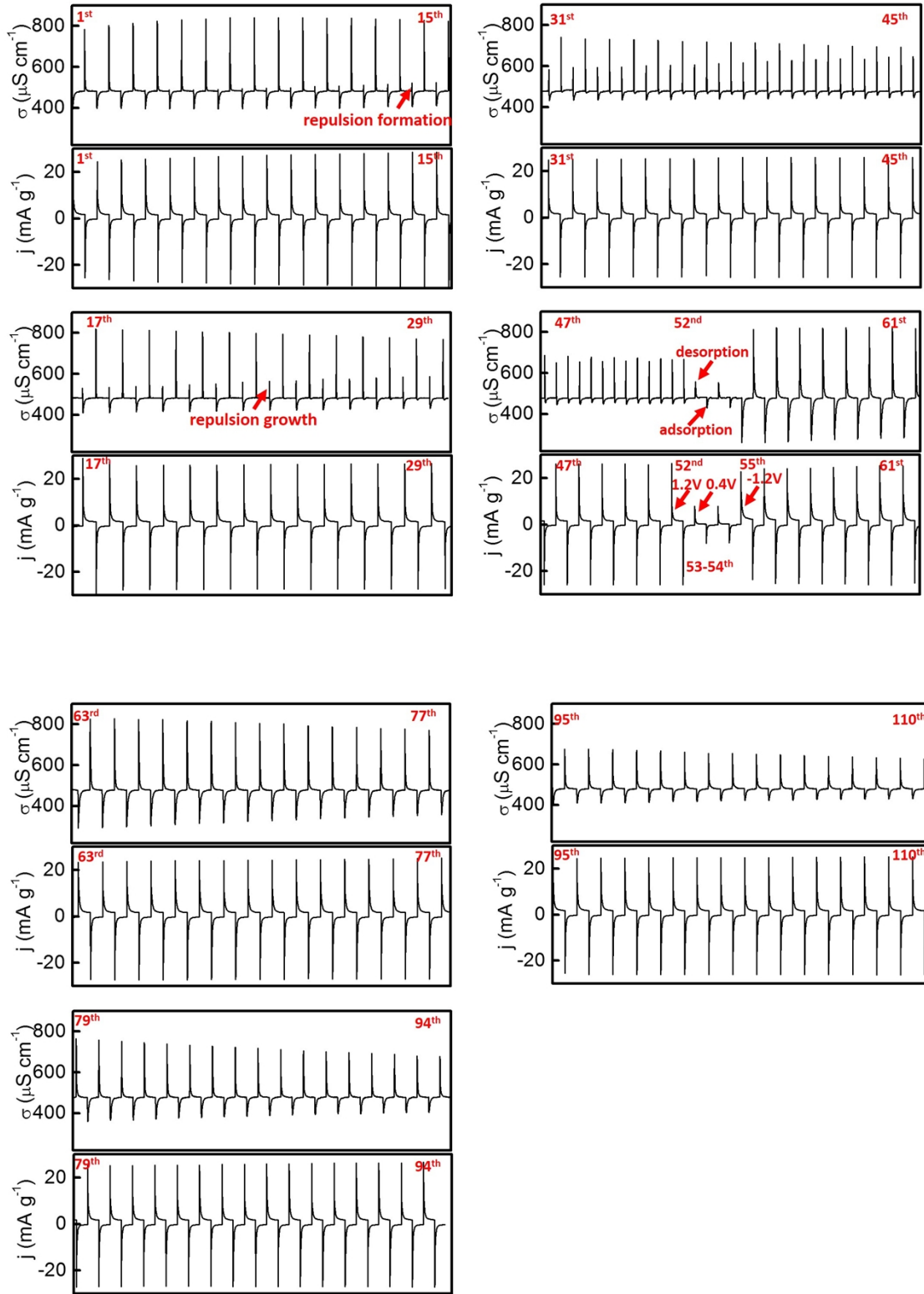
$$(E - E_{pzc}) = k_1(pH_{pzc} - pH) \quad [2a]$$

$$\zeta = k_2(pH_{pzc} - pH) \quad [2b]$$

where E and pH are the potential at an electrode and pH of the solution, respectively. k_1 and k_2 are positive constants.^{17, 18}

At fixed E and pH values in Eq. [2a], it can be predicted that an increase in the E_{PZC} value leads to a decrease in the pH_{PZC} value. Since positive shifting of the E_{PZC} has been depicted in Fig. S5, it can be understood that oxides at the carbon surface will have a negative impact on the pH_{PZC} value. This understanding has been experimentally validated by Bayram and Ayranci when SC materials were investigated for electrosorption.¹⁹ Following from Eq. [2b], at a fixed pH value, a decrease in the pH_{PZC} value leads to a decrease in the ζ value. Therefore, it can be further understood that oxides at the carbon surface will have a reduced ζ value. As the ζ -potential is a result of the net charge in the interfacial double layer,²⁰ the reduced ζ value indicates an increase in the net negative charges on the modified carbon surface. By FTIR spectra for the HNO_3 -treated CX materials, it is known that these net negative charges are the result of $-COO^-$ from the hydrolysis of $-COOH$.

According to Fig. 5(b) in the main text, we report that at 0.8 V applied from a power source, the distributed potential at the anode is ~ 0.54 V vs. SCE in 4.3 mM NaCl solution. This potential is greater than the potential for carbon oxidation (i.e., the standard potential for carbon oxidation in acidic media at $25^\circ C$ is ~ 0 V vs. SCE).²¹ Because of the existence of this driving force for oxidation, the E_{PZC} of the anode is positively shifted.



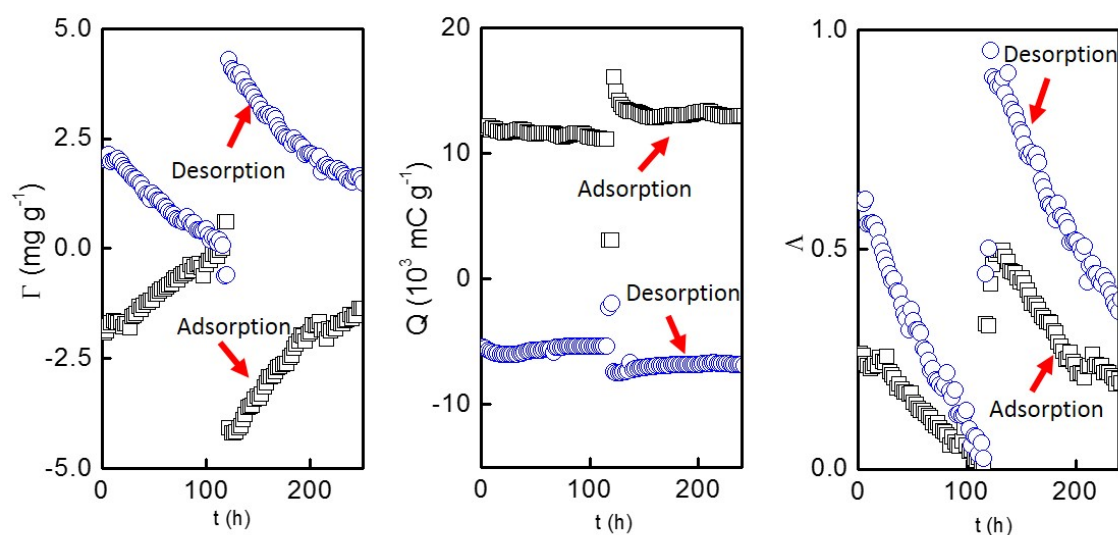


Figure S6. A CDI cell assembled with 16 pairs of pristine CX electrodes was consequently cycled at 1.2/0 V (data have been shown in the main text), 0.4/0 V, and -1.2/0 V in 31 L of 4.3 mM deaerated NaCl solution at 75 mL min⁻¹. In this plot, we show the conductivity (σ) and the corresponding current density (j). Based upon the σ and j values, the electroadsorption capacity (Γ), charge passed (Q), and charge efficiency (Λ) during the adsorption and desorption steps were quantified via Eq. [1] – [2] shown in the main text.

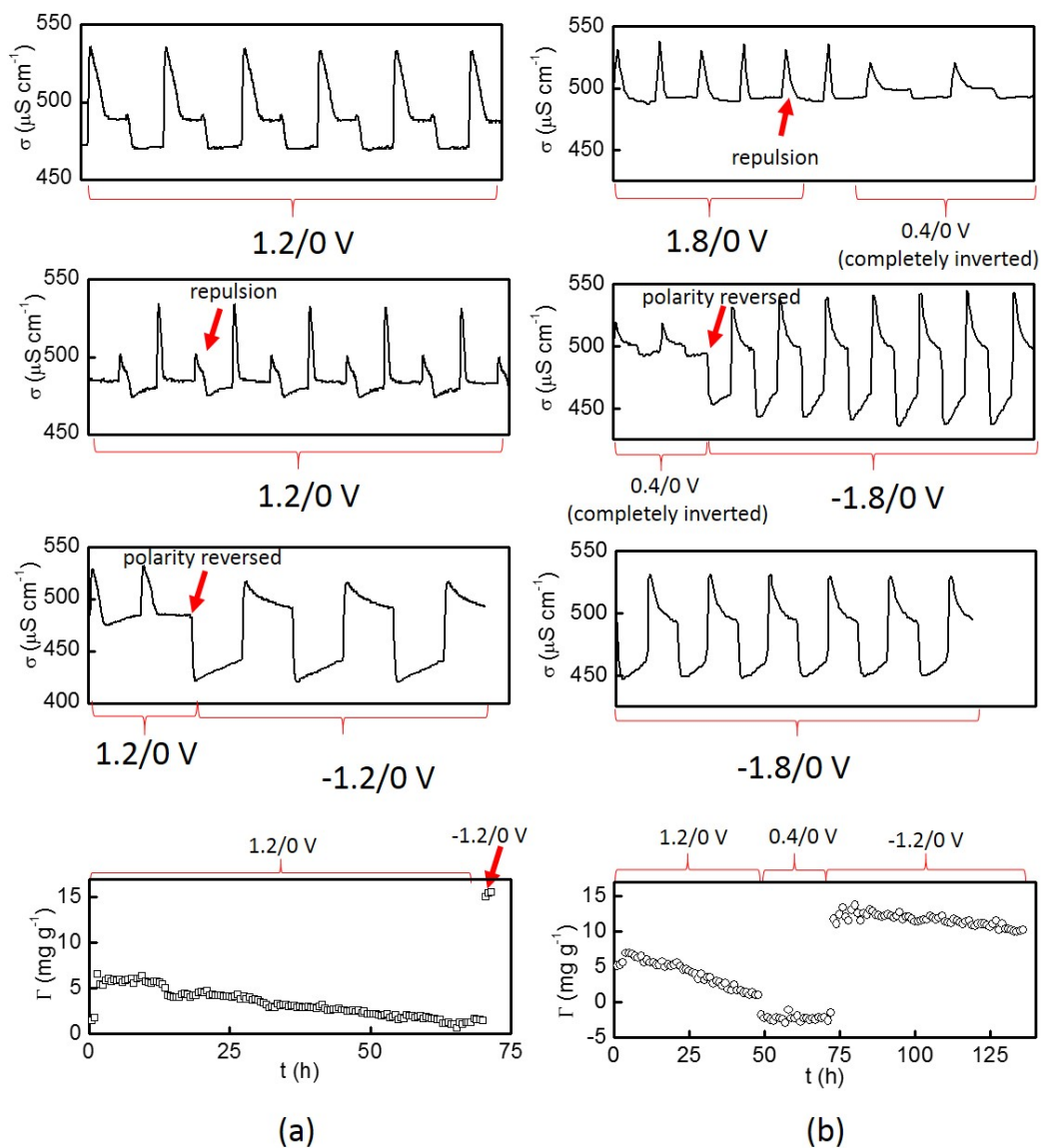


Figure S7. A CDI cell assembled with 4 pairs of (a) SC and (b) ZX electrodes was cycled at 1.2/0 V and 1.8/0 V, respectively, in 2 L of 4.3 mM deaerated NaCl solution at 75 mL min^{-1} . In general, CDI cells with ZX and SC electrodes have similar performance variation as shown earlier for that with CX electrodes in Fig. S6.

3.4. Cycling CDI Systems

3.4.1. Pristine Cathode and Anode

In our earlier work, we used a small CDI cell (i.e., 4 pairs of CX electrodes (~4 g) in 2 L of 4.3 mM deaerated NaCl solution) to study long-term cycling performance at $\pm 1.2/0$ V and $0.4/0$ V in detail.⁹ In the present work, we repeated similar testing procedures using a moderately scaled-up setup (i.e., 16 pairs of electrodes (~16 g) in 31 L of 4.3 mM deaerated NaCl solution) to verify previous results. Characteristics consistent with previous results (e.g., conductivity) are presented in Fig. S6. Briefly, at $1.2/0$ V (1st – 52nd), a repulsion (desorption) spike is observed at the beginning of each adsorption step, and the electrosorption capacity (Γ) and charge efficiency (Λ) degrade with an increasing number of cycles, but the charge passed is maintained. At $-1.2/0$ V (55th – 110th), adsorption-desorption is substantially boosted at the beginning, but performance degradation resumes with continued cycling. Additionally, at $0.4/0$ V (53rd – 54th), totally inverted adsorption-desorption behavior is observed. Furthermore, these characteristics can also be observed in Fig. S7 when the commercially available ZX and SC electrodes were cycled in a CDI cell. These characteristics are primarily related to anode oxidation due to using a potential at which the carbon electrode slowly reacts with dissolved oxygen and/or water.¹⁵ In turn, this procedure results in the relocation of the E_{PZC} of the anode and interferes with the potential distribution in a CDI cell.

According to both the mechanism developed by Avarham et al. and our early understanding using a four-electrode cell setup^{9, 22, 23}, a schematic in Fig. S8 summarizes the effect of E_{PZC} relocation on CDI performance during long-term operation using CX materials. At the beginning, both E_{PZC} s for the pristine electrodes are located in the

cathodic working domain, which means that a part of the driving force ($|E_{PZC-} - E_0|$) at the cathode is consumed by parasitical anion adsorption-desorption. During operation, the E_{PZC} for the cathode (E_{PZC-}) is almost stationary whereas the E_{PZC} for the anode (E_{PZC+}) is shifted into the anodic working domain. Thus, the driving force created ($|E_{PZC+} - E_0|$) for cation adsorption-desorption paired with the present driving force ($|E_{PZC-} - E_0|$) for anion adsorption-desorption contributes to the repulsion spikes observed (This inversion spike can also be found in Fig. S7 and S9 when a CDI cell was operated under different conditions, e.g., different applied voltages and different carbon electrodes used). With polarity reversal, both E_{PZCS} are placed beyond their respective working domains. Therefore, the highest performance should be obtained when the polarity of the electrodes are reversed.²⁴ During extended cycles, due to carbon oxidation at the anode, the E_{PZC} for the new anode (prior cathode) is relocated into its respective working domain, but the E_{PZC} for the new cathode (prior anode) remains at nearly the same location due to insufficient reducing potentials at the cathode to negatively shift the E_{PZC} . Thus, the E_{PZC} for both electrodes are eventually located in the anodic working domain. Under such a condition, the performance is limited at the anode, which is opposite to the beginning.

In summary, we conclude that performance degradation is nearly always related to E_{PZC} relocation due to electrochemical oxidation at the anode, which agrees with Cohen et al. that the minimization of anode oxidation is one of the key challenges for further development of carbon electrodes for CDI applications.²⁵

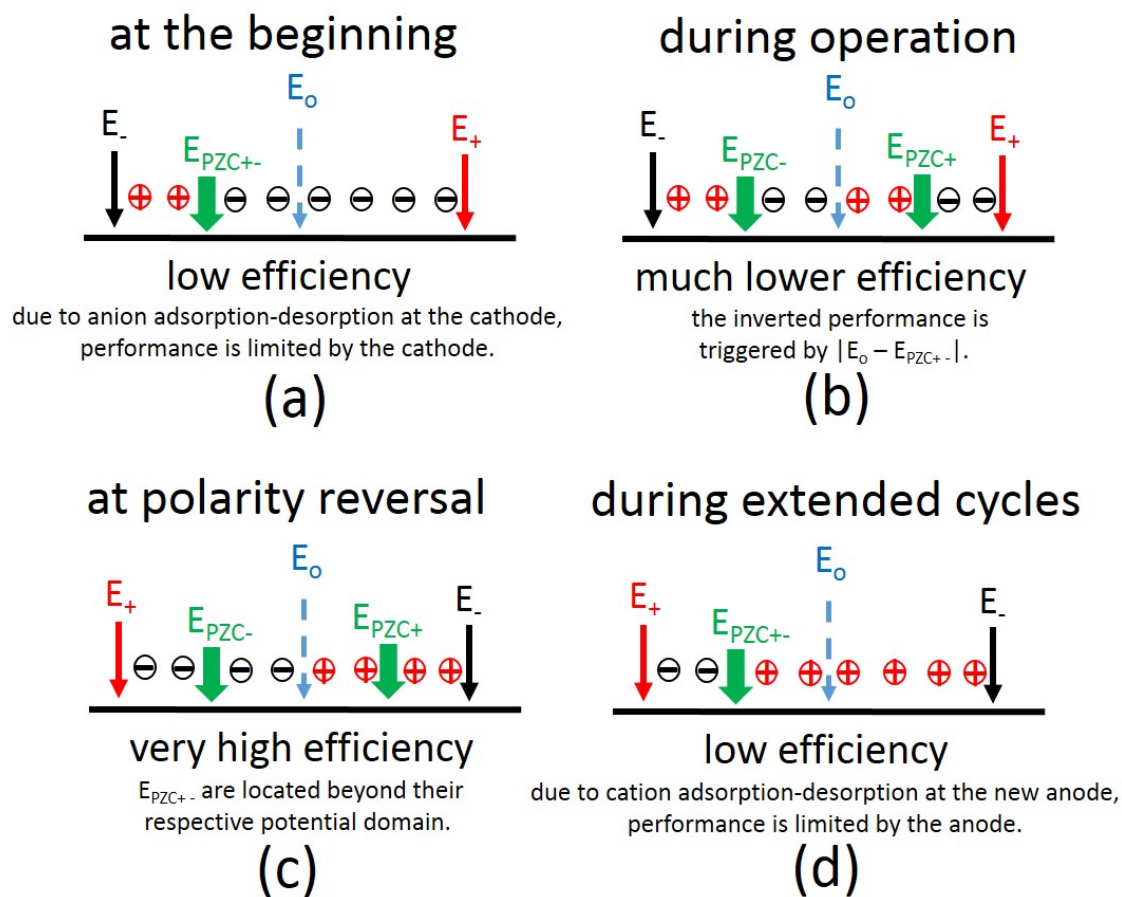


Figure S8. A schematic illustration of the mechanism for the performance variation according to Fig. S6-7.

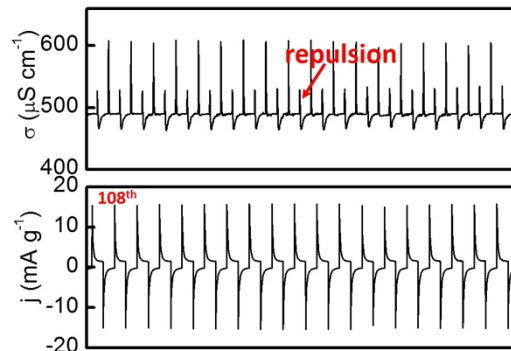
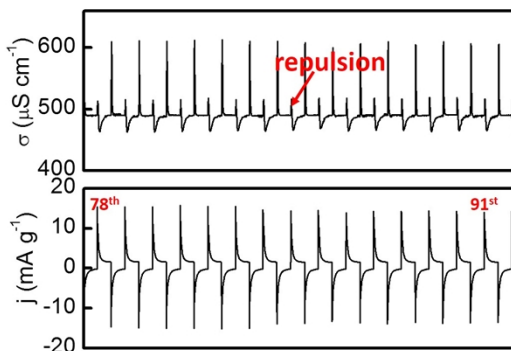
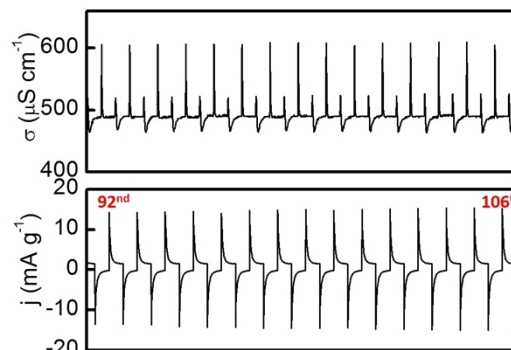
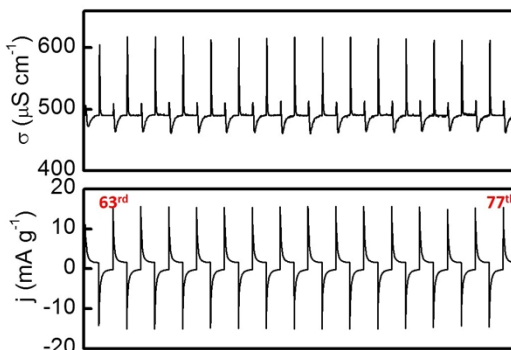
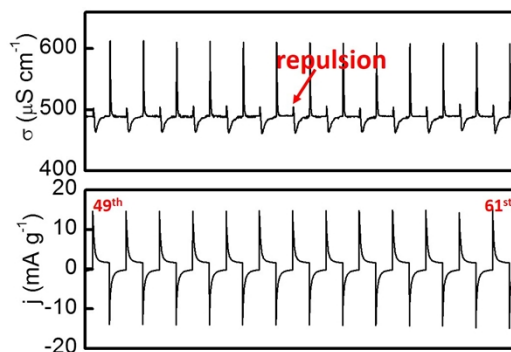
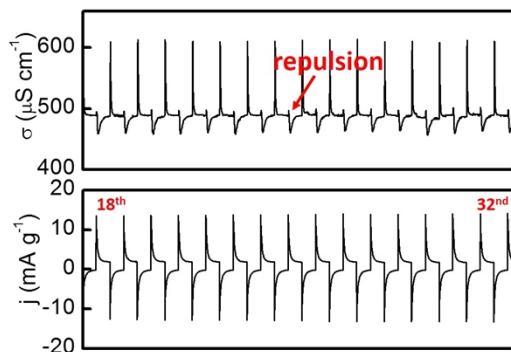
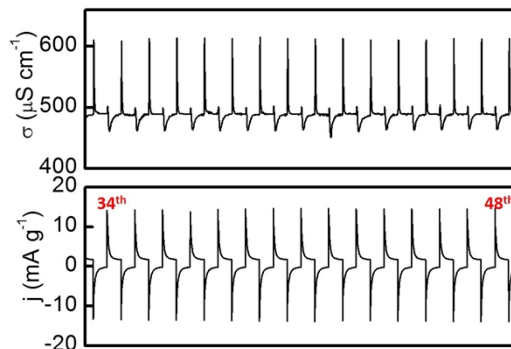
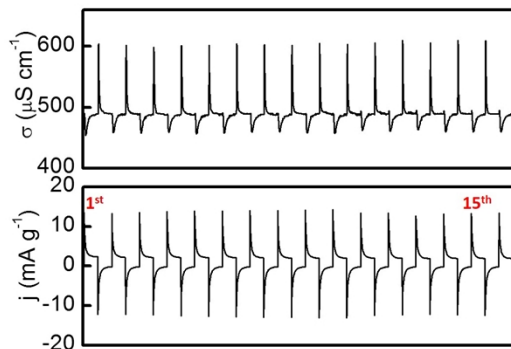


Figure S9. A CDI system assembled with 16 pairs of CX electrodes was consequently cycled at 0.8/0 V, in 31 L of 4.3 mM deaerated NaCl solution at 75 mL min⁻¹. The performance evaluation has been shown in the main text.

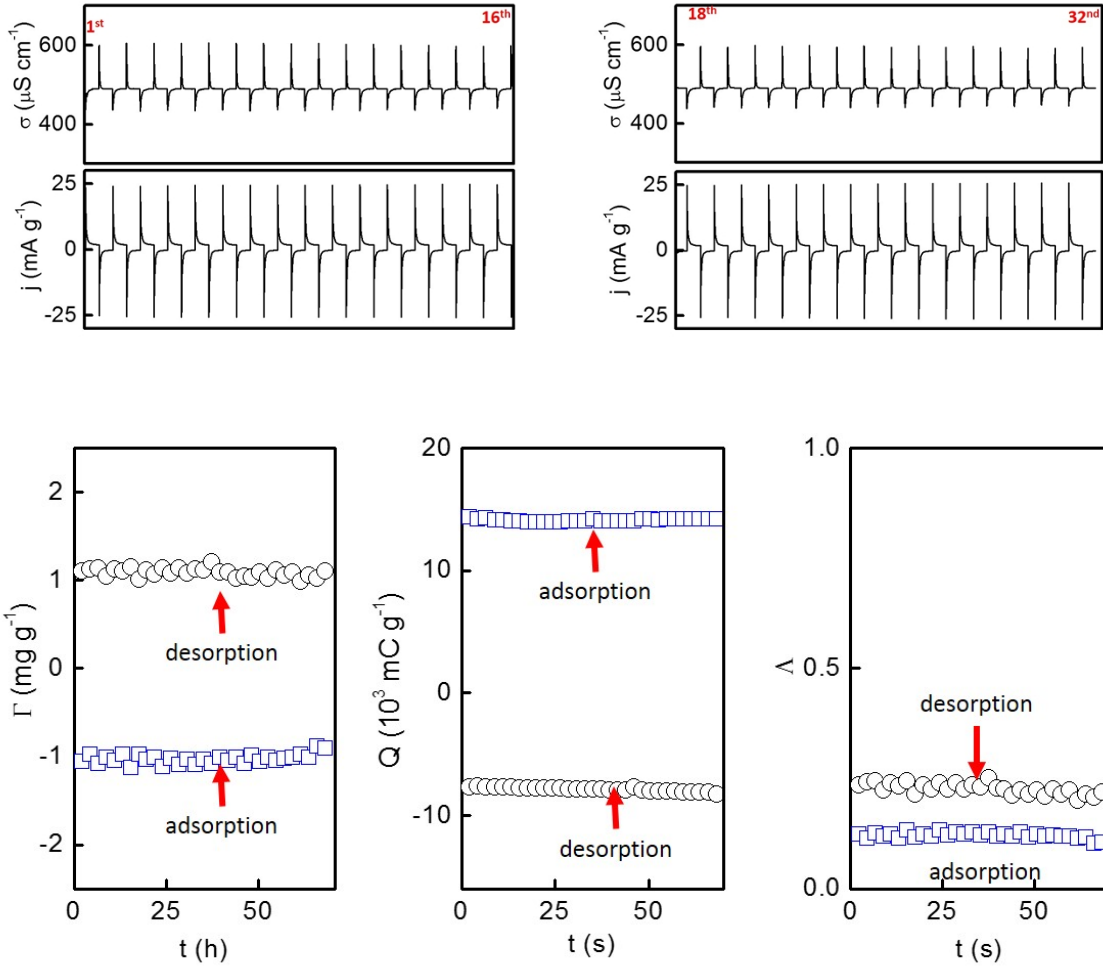
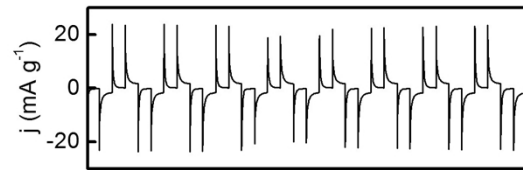
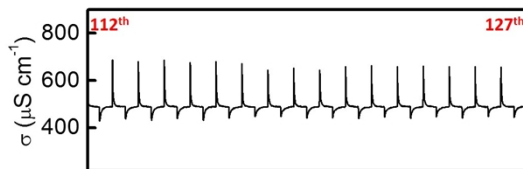
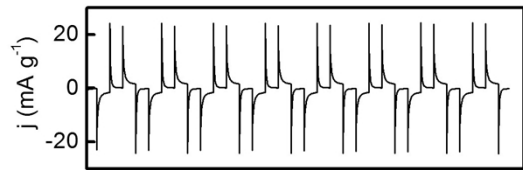
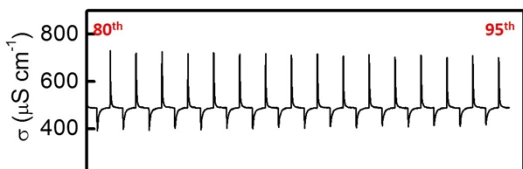
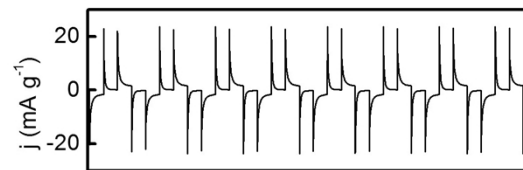
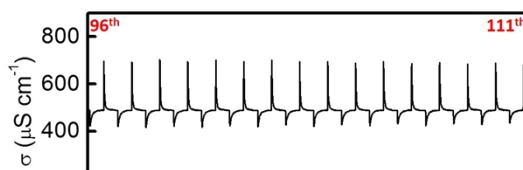
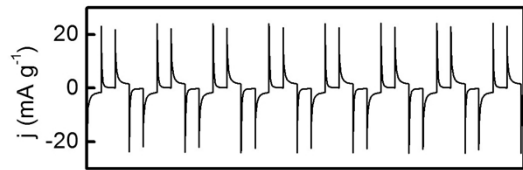
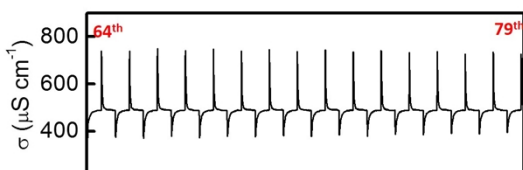
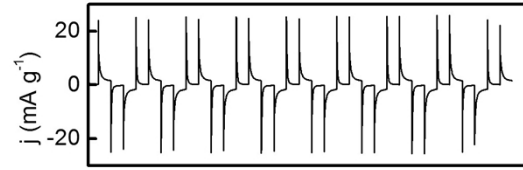
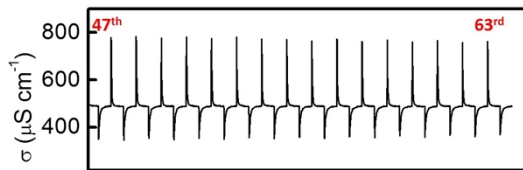
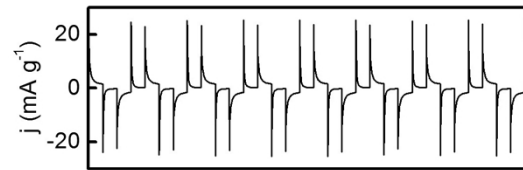
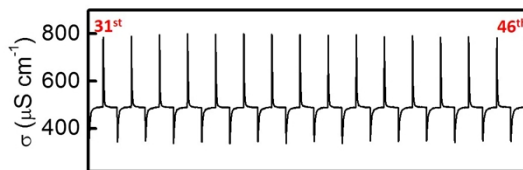
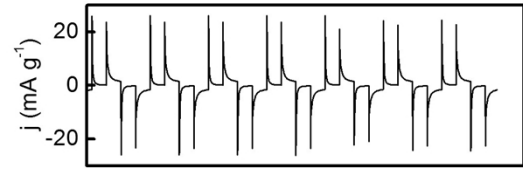
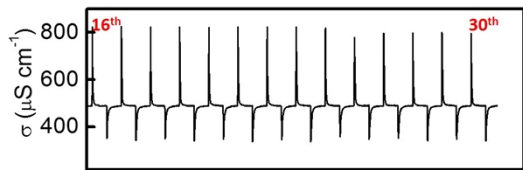
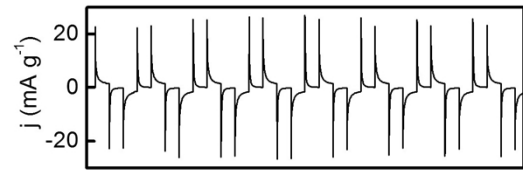
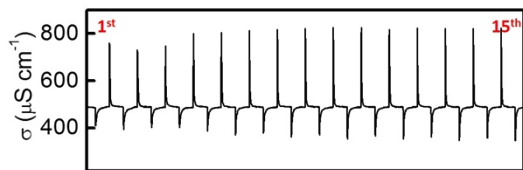


Figure S10. A CDI system assembled with 16 pairs of HNO₃-treated CX electrodes was cycled at 1.2/0 V, in 31 L of 4.3 mM deaerated NaCl solution at 75 mL min⁻¹. In this plot, we show the conductivity (σ) and the corresponding current density (j). Based upon the σ and j values, the electroadsorption capacity (Γ), charge passed (Q), and charge efficiency (Λ) during the adsorption and desorption steps were quantified via Eq. [1] – [2] shown in the main text.

3.4.2. Oxidized Cathode and Anode

A cycling test was performed using 16 pairs of HNO₃-treated electrodes at 1.2/0 V operation in 31 L of 4.3 mM deaerated NaCl solution at 75 mL min⁻¹. Fig. S10 shows that inversion/repulsion does not take place during the cycling test (about 75 hours), but the desalination performance is limited by the performance at the anode under such a condition.⁹



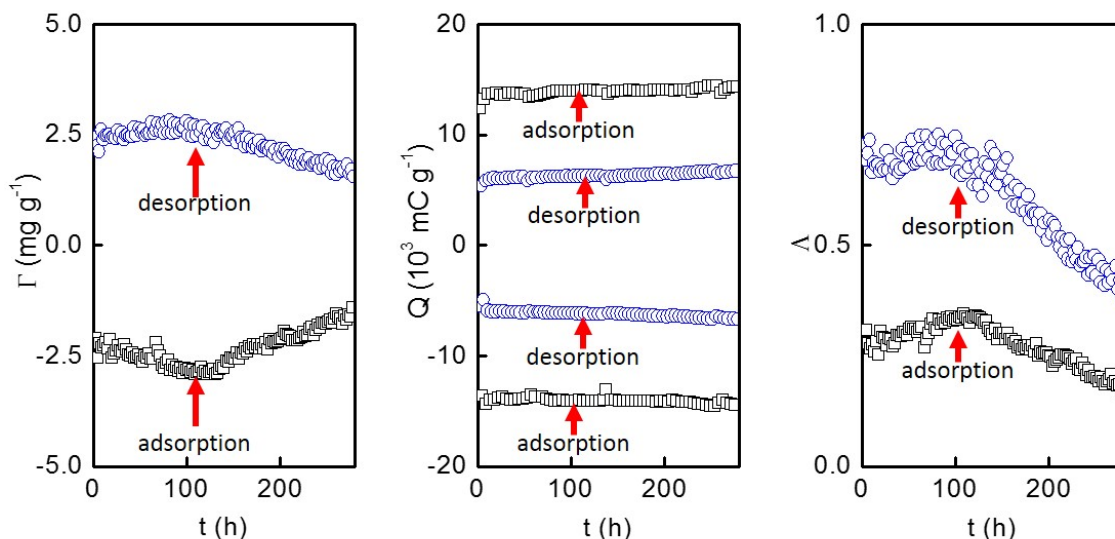


Figure S11. A CDI cell assembled with 16 pairs of pristine CX electrodes was operated at $\pm 1.2/0$ V (i.e., reversing the polarity after every cycle) in 31 L of 4.3 mM deaerated NaCl solution at 75 mL min^{-1} . In this experiment, except for the charging method, the experimental conditions were kept the same as that shown in Fig. S6. In this plot, we show the conductivity (σ) and the corresponding current density (j). Based upon the σ and j values, the electroadsorption capacity (Γ), charge passed (Q), and charge efficiency (Λ) during the adsorption and desorption steps were quantified via Eq. [1] – [2] shown in the main text.

3.4.3. Constant-Voltage Switching after Every Cycle

In order to verify the conclusion drawn recently by Cohen et al.,²⁶ we performed another cycling test at $\pm 1.2/0$ V (i.e., reversing the polarity after every cycle) in 31 L of 4.3 mM deaerated NaCl solution at 75 mL min^{-1} . Fig. S11 shows the conductivity, current density, and performance evaluations. Compared to the performance evaluations shown in Fig. S6, it is found that no repulsion peak was formed at the beginning of each charging step

for the entire operation at $\pm 1.2/0$ V. Therefore, it can be concluded that the constant-voltage switching method can significantly extend the life span of a CDI cell. For example, the CDI cell operated at $1.2/0$ V displays the complete loss in electrosorption capacity (Γ) within approximately 100 hours whereas operation at $\pm 1.2/0$ V was maintained in the first 100 hours. However, during extended cycles, performance degradation is still observed. This degradation is mainly attributed to the E_{PZC} for both the electrodes being shifted into the anodic working voltage window based upon the mechanism shown in Fig. S8.

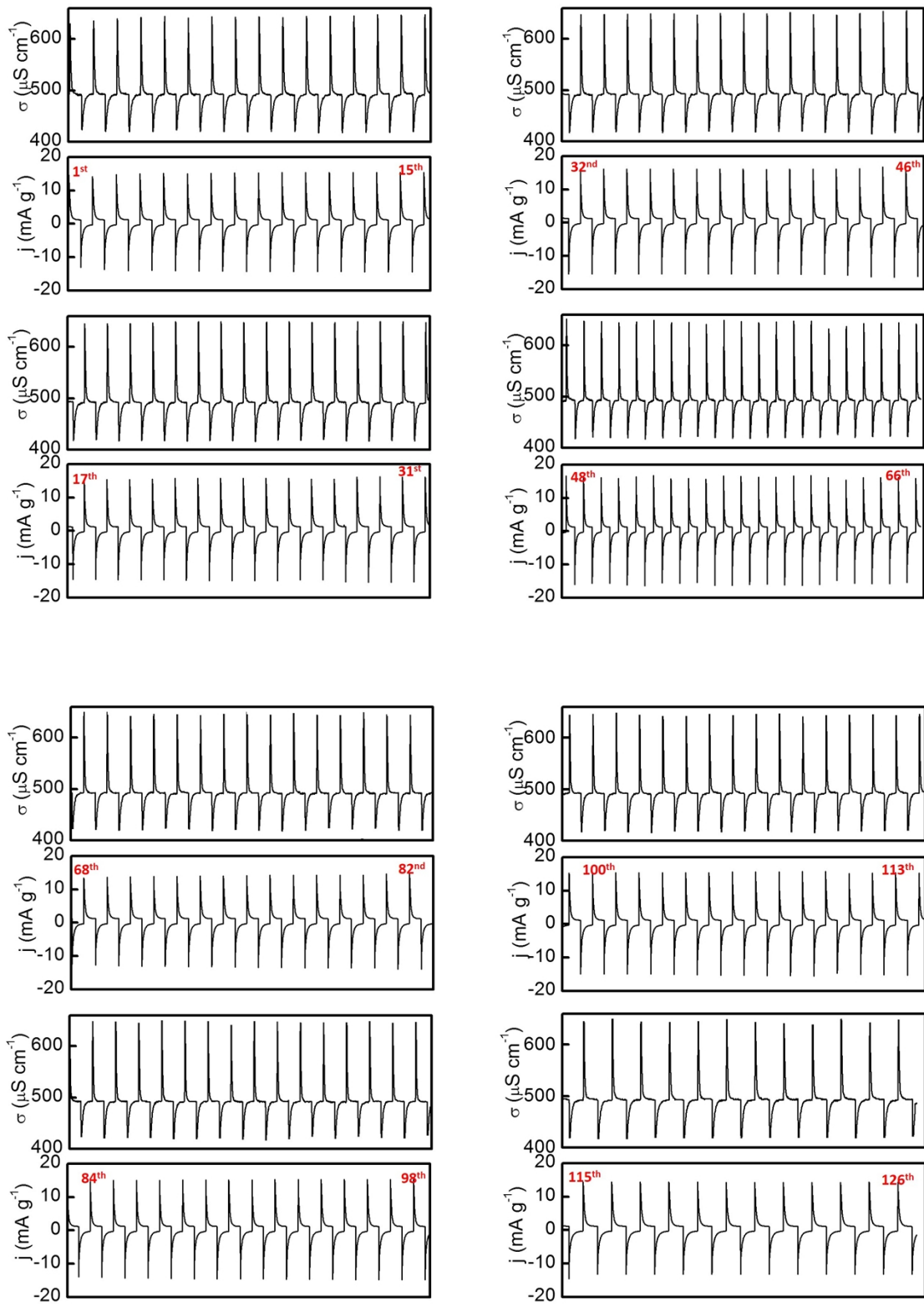


Figure S12. An i-CDI system assembled with 16 pristine CX cathodes and 16 Si-CX anodes was cycled at 0.8/0 V in 31 L of 4.3 mM deaerated NaCl solution at 75 mL min⁻¹. The performance evaluation has been shown in the main text.

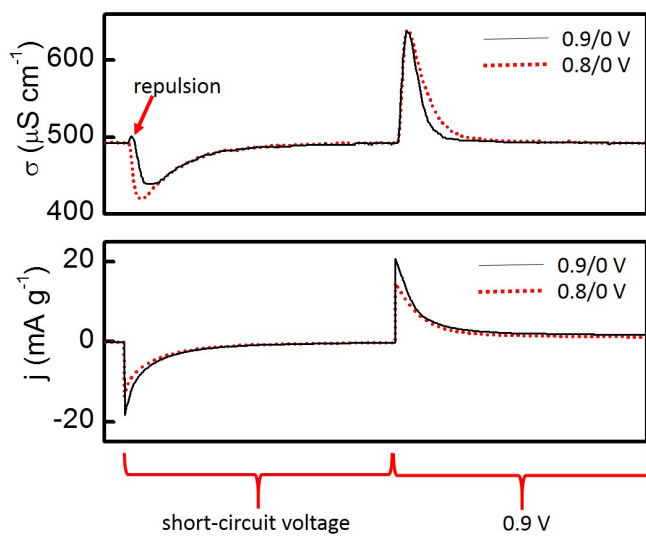


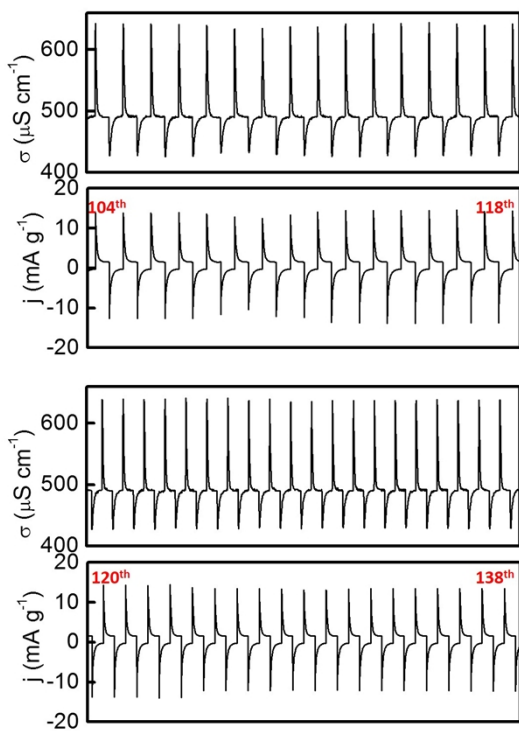
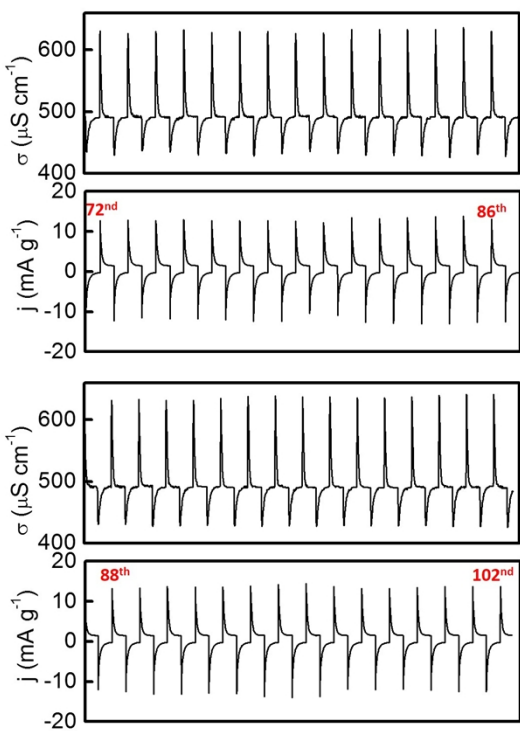
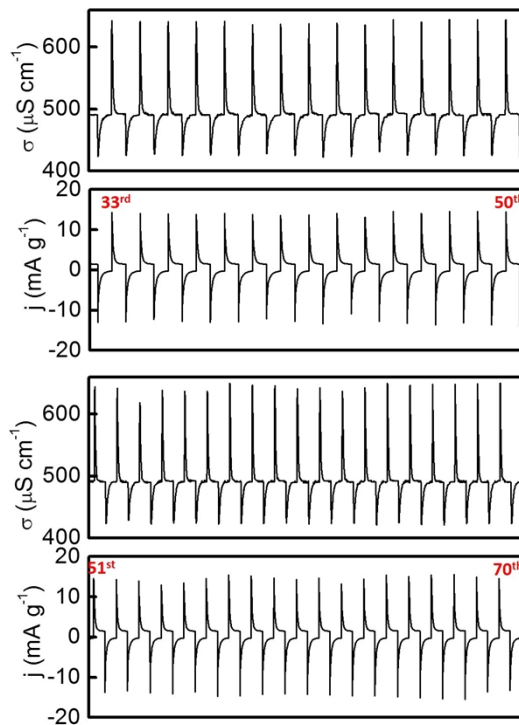
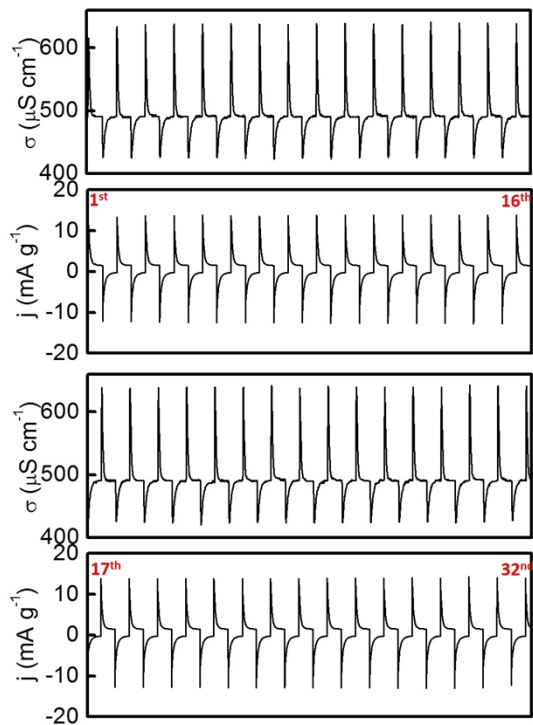
Figure S13. A selected cycle at 0.9/0 V was performed in 31 L of 4.3 mM deaerated NaCl solution at 75 mL min⁻¹ using an i-CDI cell with 16 pristine CX cathodes and 16 Si-CX anodes. One cycle at 0.8/0 V was overlaid for comparison.

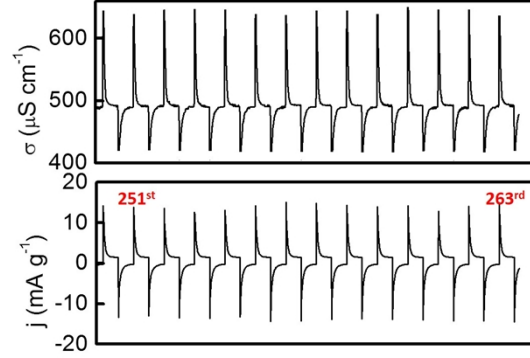
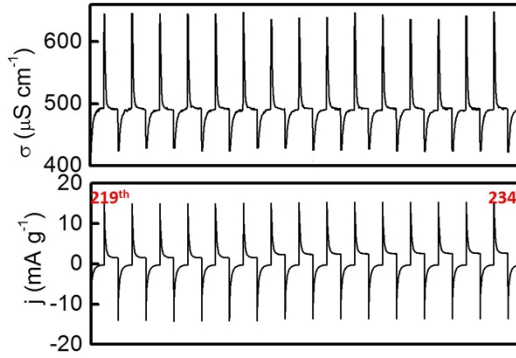
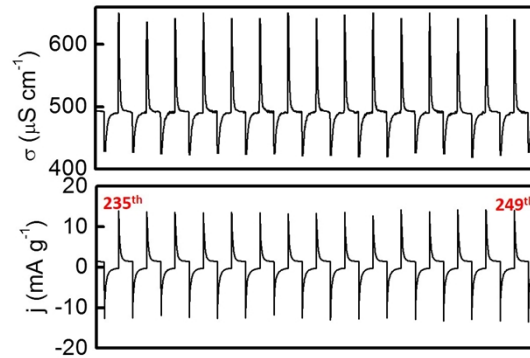
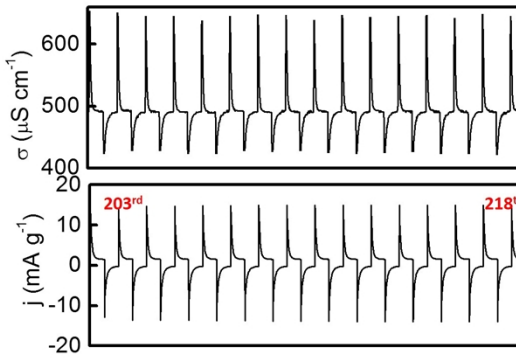
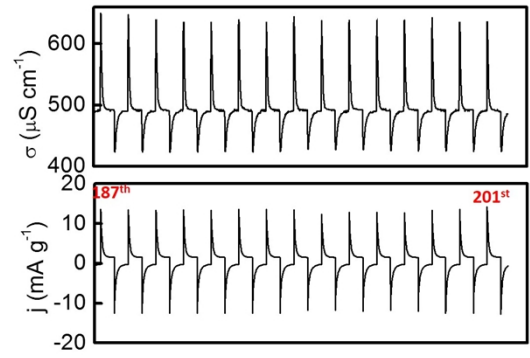
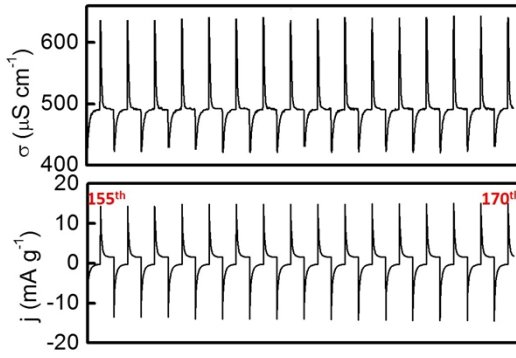
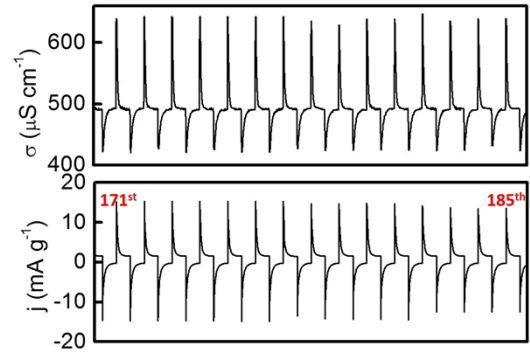
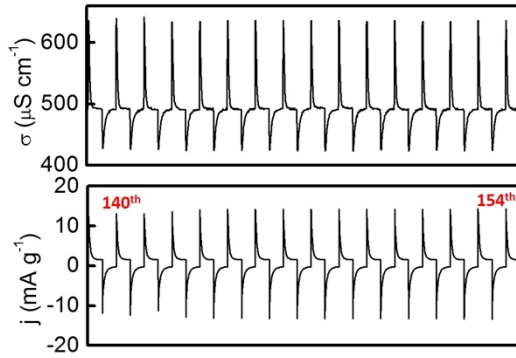
3.5. Cycling i-CDI Systems

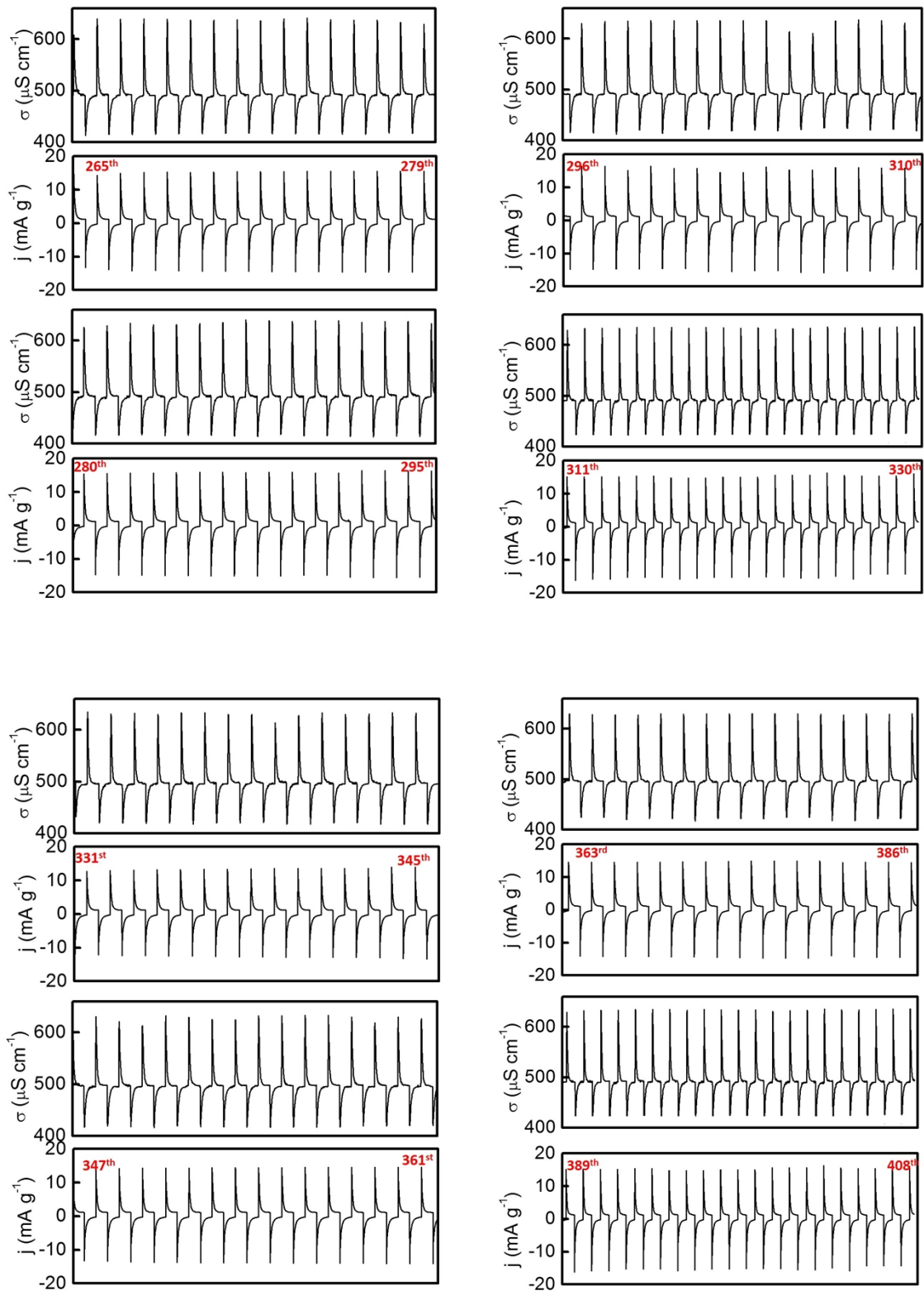
Figure S12 shows an i-CDI cell with 16 pristine CX cathodes and 16 Si-CX anodes was cycled at 0.8/0 V in 31 L of 4.3 mM deaerated NaCl solution at 75 mL min⁻¹. The performance evaluation has been shown in the main text. It is also found in Fig. S13 that during the discharging step (i.e., short-circuit) for a cell operated at 0.9/0 V, an ion repulsion peak highlighted by an arrow is observed. This is due to the smaller amount of

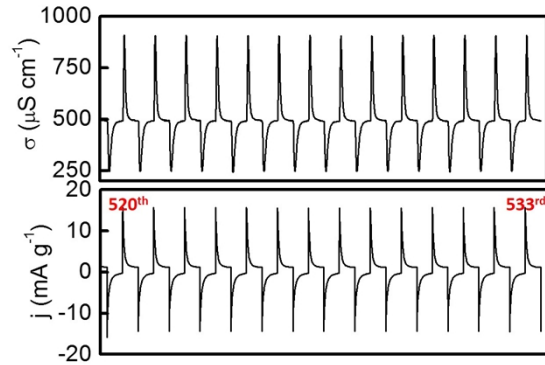
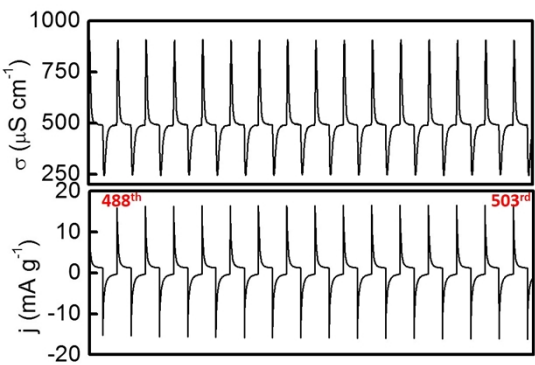
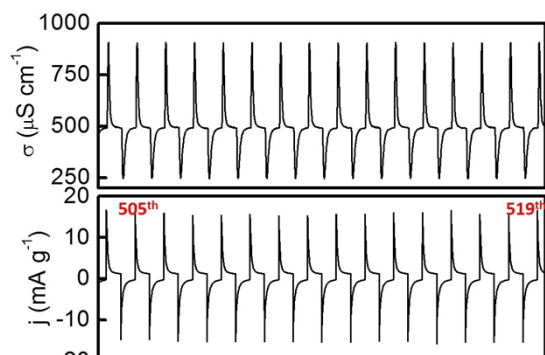
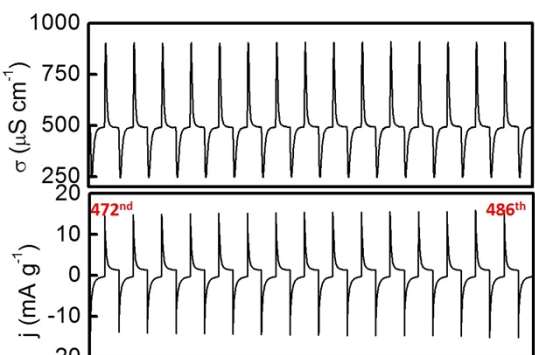
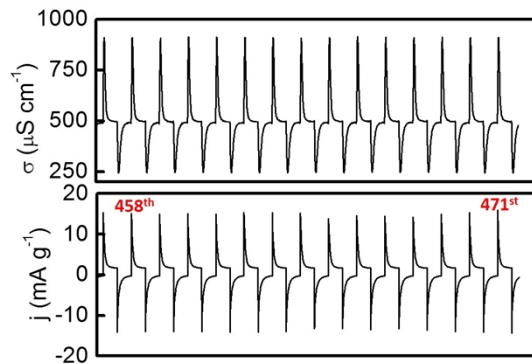
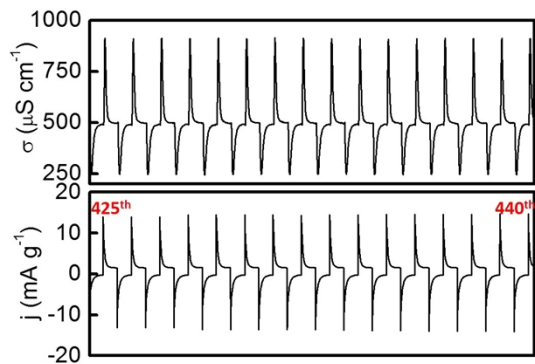
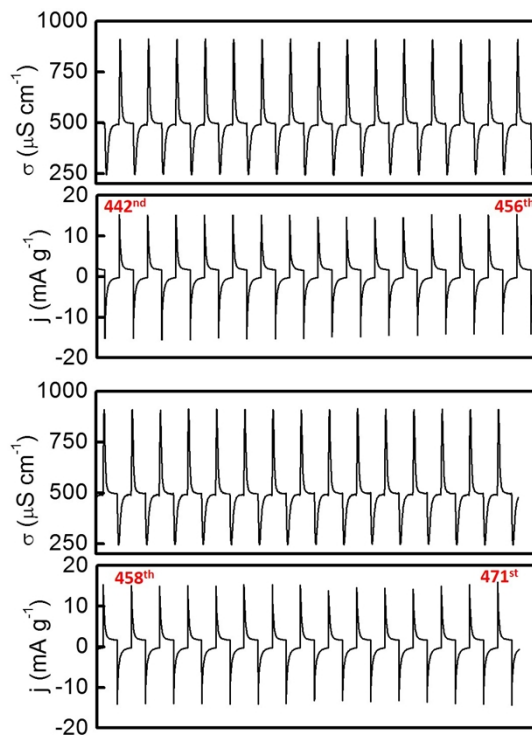
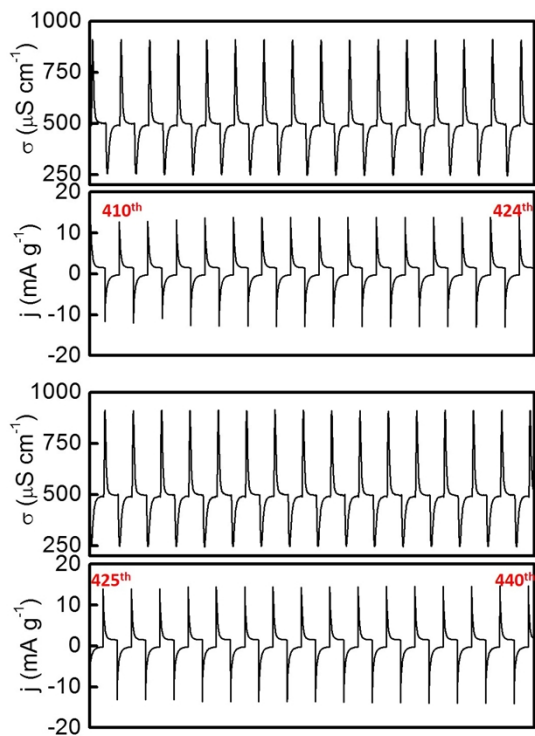
salt that is desorbed when the CDI cell was charged at 0.9 V. As a consequence, a future possible study could be conducted to examine the electrosorption capacity and charge efficiency of carbon electrodes with either more positive or negative E_{PZCS} to expand the internal potential window for the i-CDI system.

Recently, the i-CDI method was re-evaluated using CX as the cathode and Si-CX as the anode for a CDI cell in 31 L of 4.3 mM deaerated NaCl solution at 75 mL min⁻¹ for ~450 hours (1st – 408th cycle) and at 25 mL min⁻¹ for another ~200 hours (409th – 593rd cycle). Very stable desalination performance is shown in Fig. S14. It can be concluded that use of the i-CDI method can effectively extend the lifespan of a desalination device.









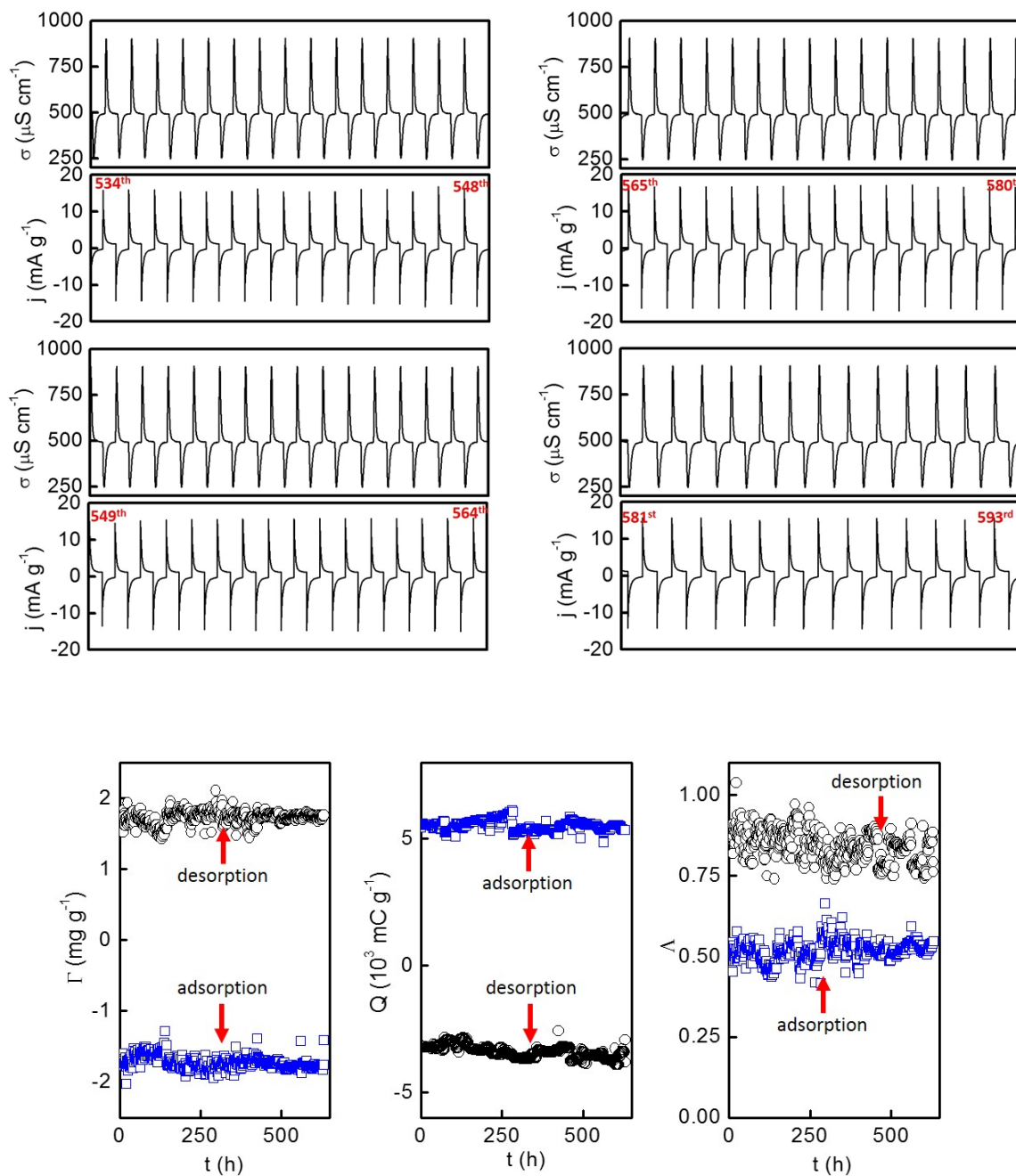


Figure S14. An i-CDI system assembled with 16 pristine CX cathodes and 16 Si-CX anodes was cycled at 0.8/0 V in 31 L of 4.3 mM deaerated NaCl solution at 75 mL min^{-1} for ~ 450 hours (1st – 408th cycle) and at 25 mL min^{-1} for another ~ 200 hours (409th – 593rd cycle). Performance metrics including the electroadsorption capacity (Γ), charge passed (Q), and charge efficiency (Λ) have also been evaluate.

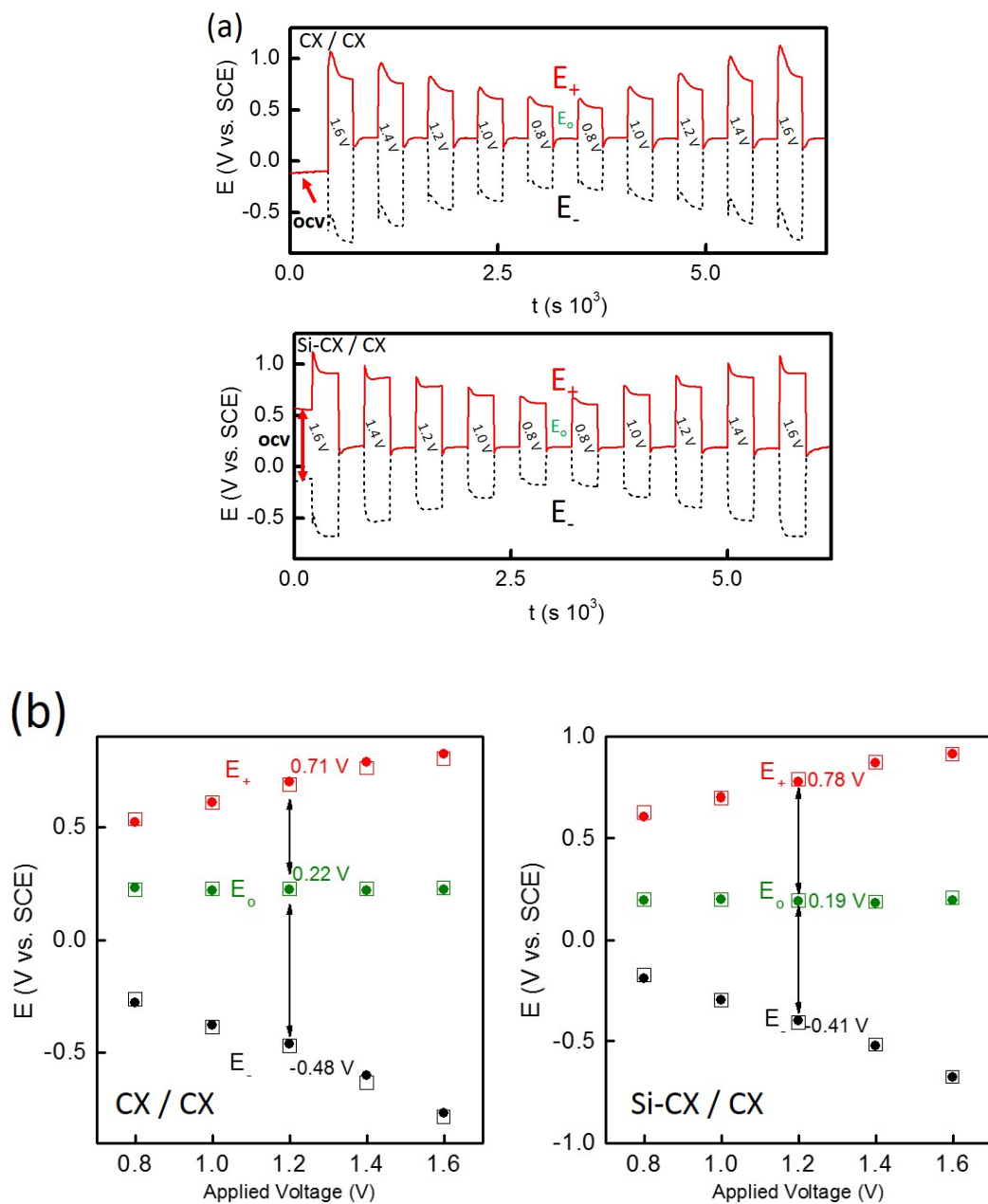


Figure S15. Characterizations using a four-electrode setup in 4.3 mM deaerated NaCl. In this plot, CX/CX represents a pair of pristine CX electrodes, and Si-CX/CX denotes Si-CX anode and CX cathode. (a) The potential distribution was measured at applied voltages between 0.8-1.6 V. (b) A plot of the potential at each electrode as a function of

the applied voltage. The potential data (last 60s) shown in Fig. S15(a) were taken to calculate the average data shown in Fig. S15(b).

3.6. Potential Distribution Measurements

Fig. S15(a) shows the potential distribution measurements with both descending and ascending potentials between 0.8-1.6 V in 4.3 mM deaerated NaCl. It is found that the open-circuit voltage (OCV) for the Si-CX electrode is natively greater than that for the CX electrode. Fig. S15(b) shows the plot of the potential at each electrode as a function of the applied voltage. It is found that the cell configured with the Si-CX electrode (anode) and the CX electrode (cathode) has much more even distributed potentials compared to that with a pair of pristine CX electrodes.

References

1. P. A. Webb, C. Orr, R. W. Camp, J. P. Olivier and Y. S. Yunes, *Analytical Methods in Fine Particle Technology*, Micromeritics Instrument, 1997.
2. A. J. Bard and L. R. Faulkner, *Electrochemical Methods - Fundamentals and Applications*, John Wiley & Sons, New York, 2001.
3. C.-H. Hou, C. Liang, S. Yiacoumi, S. Dai and C. Tsouris, *J. Colloid Interface Sci.*, 2006, **302**, 54-61.
4. D. C. Grahame, *Chem. Rev.*, 1947, **41**, 441-501.
5. L.-H. Shao, J. Biener, D. Kramer, R. N. Viswanath, T. F. Baumann, A. V. Hamza and J. Weissmuller, *Phys. Chem. Chem. Phys.*, 2010, **12**, 7580-7587.
6. M. Hahn, M. Baertschi, O. Barbieri, J.-C. Sauter, R. Kötz and R. Gally, *Electrochem. Solid-State Lett.*, 2004, **7**, A33-A36.
7. M. D. Levi, S. Sigalov, G. Salitra, R. Elazari and D. Aurbach, *J. Phys. Chem. Lett.*, 2011, **2**, 120-124.
8. M. D. Levi, S. Sigalov, D. Aurbach and L. Daikhin, *J. Phys. Chem. C*, 2013, **117**, 14876-14889.

9. X. Gao, A. Omosebi, J. Landon and K. Liu, *J. Electrochem. Soc.*, 2014, **161**, E159-E166.
10. X. Gao, A. Omosebi, J. Landon and K. Liu, *Electrochem. Commun.*, 2014, **39**, 22-25.
11. K.-L. Yang, S. Yiacoumi and C. Tsouris, *J. Electroanal. Chem.*, 2003, **540**, 159-167.
12. R. K. Kalluri, M. M. Biener, M. E. Suss, M. D. Merrill, M. Stadermann, J. G. Santiago, T. F. Baumann, J. Biener and A. Striolo, *Phys. Chem. Chem. Phys.*, 2013, **15**, 2309-2320.
13. B. Stuart, *Infrared Spectroscopy: Fundamentals and Applications*, Wiley, 2004.
14. S. Yang, X. Li, W. Zhu, J. Wang and C. Descorme, *Carbon*, 2008, **46**, 445-452.
15. K. Kinoshita, *Carbon - Electrochemical and Physicochemical Properties*, John Wiley & Sons, New York, 1988.
16. H. Tobias and A. Soffer, *J. Electroanal. Chem. Interfacial Electrochem.*, 1983, **148**, 221-232.
17. E. McCafferty, *Electrochim. Acta*, 2010, **55**, 1630-1637.
18. P. H. Tewari and A. W. McLean, *J. Colloid Interface Sci.*, 1972, **40**, 267-272.
19. E. Bayram and E. Ayrançi, *Carbon*, 2010, **48**, 1718-1730.
20. A. D. McNaught and A. D. McNaught, *Compendium of chemical terminology*, Blackwell Science Oxford, 1997.
21. J. R. Varcoe, P. Atanassov, D. R. Dekel, A. M. Herring, M. A. Hickner, P. A. Kohl, A. R. Kucernak, W. E. Mustain, K. Nijmeijer, K. Scott, T. Xu and L. Zhuang, *Energy Environ. Sci.*, 2014, **7**, 3135-3191.
22. E. Avraham, M. Noked, I. Cohen, A. Soffer and D. Aurbach, *J. Electrochem. Soc.*, 2011, **158**, P168-P173.
23. I. Cohen, E. Avraham, M. Noked, A. Soffer and D. Aurbach, *J. Phys. Chem. C*, 2011, **115**, 19856-19863.
24. Y. Bouhadana, E. Avraham, A. Soffer and D. Aurbach, *Aiche J.*, 2010, **56**, 779-789.
25. I. Cohen, E. Avraham, Y. Bouhadana, A. Soffer and D. Aurbach, *Electrochim. Acta*, 2013, **106**, 91-100.
26. I. Cohen, E. Avraham, Y. Bouhadana, A. Soffer and D. Aurbach, *Electrochim. Acta*, 2015, **153**, 106-114.